

Prussian Blue Nanohybridized Multicellular Spheroids as Composite Engraftment for Antioxidant Bone Regeneration and Photoacoustic Tomography

Lu Chen, Shijia Tang, Jiamin Zhang, Caiying Zhong, Xueqin Xu, Jia Yan, Ke Hu,* Zhaobin Guo, and Feimin Zhang*



Cite This: <https://doi.org/10.1021/acsnano.3c06835>



Read Online

ACCESS |

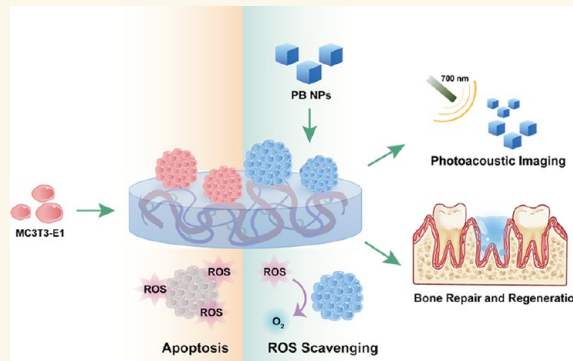
Metrics & More

Article Recommendations

Supporting Information

ABSTRACT: Regulating the complex microenvironment after tooth extraction to promote alveolar bone regeneration is a pressing challenge for restorative dentistry. In this study, through modulating the mechanical properties of the cellular matrix, we guided various types of cells by self-organizing to form multicellular spheroids (MCSs) and hybridized MCSs with Prussian Blue nanoparticles (PBNPs) in the process. The constructed Prussian Blue nanohybridized multicellular spheroids (PBNPs@MCSs) with empowered antioxidant functions effectively reduced cell apoptosis under peroxidative conditions and exhibited enhanced ability to regulate the microenvironment and promote bone repair both in vitro and in vivo. In addition, the PBNPs@MCSs exhibited enhanced photoacoustic imaging ability to trace low doses of PBNPs. Therefore, the constructed PBNPs@MCSs based on the biomimetic hydrogel can be used as a form of an engraftment building block, with a greater potential for pro-bone repair application in the complex microenvironment of the oral cavity.

KEYWORDS: nanohybrid, Prussian Blue nanoparticles, multicellular spheroids, antioxidant and pro-bone repair, photoacoustic tomography, enhanced diagnosis and treatment



Periodontal disease, dental trauma, and maxillofacial tumors often lead to tooth extraction or loss.^{1,2} Alveolar bone resorption is a common clinical complication of tooth loss, and resorption can lead to reduced restorative outcomes, including the loss of treatment options for implant placement.^{3–5} Traditional jawbone regeneration techniques involve the application of bone graft materials with or without a barrier membrane.⁶ Bone graft materials include autografts, allografts, xenografts, and synthetic biomaterials.⁷ However, autologous grafts are more traumatic to the patient, and both allogeneic and xenograft bone grafts may produce varying degrees of antigenic reactions.⁸ An effective strategy is to repair defects in periodontal tissue and alveolar bone with cellular tissue engineering therapy, and cell-based jaw bone regeneration techniques urgently need to be developed and applied. However, the complex microenvironment and high incidence of inflammation in the oral alveolar sockets make it often difficult for cells to survive after transplantation, and the

current single-cell suspension transplantation technique is even more difficult to meet the survival rate of clinical treatment, thus limiting the final clinical restorative outcome.^{9–12} After tooth extraction, the trauma can trigger inflammatory responses; in the meantime, oral pathogens can invade tooth-supporting tissues, such as gums, periodontal ligaments, and alveolar bone, triggering immune responses characterized by overproduction of reactive oxygen species (ROS).^{13–15} The excessive production of ROS can exacerbate the inflammatory responses at the injury site and slow down the healing of bone defects.^{16–18} It has been shown that high concentrations of

Received: July 24, 2023

Revised: August 9, 2024

Accepted: August 9, 2024

ROS induce the death of osteogenic precursor cells and mature osteoblasts and inhibit the osteogenic differentiation of bone mesenchymal stem cells (BMSCs) and MC3T3-E1 cells by suppressing the expression of osteogenic markers.¹⁹ In addition, ROS act as intracellular signal transduction molecules to promote osteoclast formation, which leads to alveolar bone resorption and periodontal tissue damage.²⁰ In order to facilitate implantation and survival of implanted cells, there is an urgent need to develop a highly responsive treatment tool that can remove excess ROS to attenuate the oral inflammatory microenvironment and promote alveolar bone repair. Meanwhile, evaluation of the location and residual amount of early implanted cells is a crucial part of ensuring the sufficient efficacy of the transplanted cells,^{21,22} therefore allowing early postoperative diagnosis and effective assessment of the success of the implanted cells. Existing cell therapy with single functional implants failed to meet the actual clinical needs of bone repair.^{23,24}

A composite implant that combines microenvironmental modulation, ROS scavenging, and imaging functions can effectively address the above issues. The implant should regulate the osteogenic microenvironment after tooth loss and reduce the occurrence of inflammatory reactions in the alveolar socket. Besides, it should also minimize alveolar ridge resorption and maximize bone formation, while its position can be tracked as well. Our previous study found that multicellular spheroids (MCSs) have enhanced viability and self-renewal ability, enhanced protein expression, as well as superior therapeutic efficacy for tissue regeneration in transplantation.²⁵ In addition, Prussian Blue nanoparticles (PBNPs) have excellent mimetic enzyme activity, which can effectively scavenge ROS.^{26–28} Moreover, they have good absorption efficiency for near-infrared (NIR) laser pulses, making them an excellent photoacoustic contrast agent.²⁹ Due to the high binding affinity of PBNPs with cyanide ions, they pass harmlessly through the human body and, as a result, have better biocompatibility compared to other antioxidant nanoparticles. PBNPs are also the only commercially available agent that can be used to reduce the biological half-life of radioactive ions.^{30,31} Our group in the previous period has also done some basic research on the synthesis and preparation, biocompatibility, and stability of PBNPs.^{32,33} However, the free nanoparticles, which potentially will enter circulation and cause unexpected tissue accumulation, might generate detrimental effects on humans, albeit PBNPs have excellent biocompatibility and are approved by the FDA for clinical use.²⁶ Thus, we pioneered a method for the construction of Prussian Blue nanohybridized multicellular spheroids (PBNPs@MCSs) based on a series of previous work on bionanogel materials: cells were cultured on mechanically tunable hydrogels, and the self-organization of cells into MCSs was guided by modulating the mechanical properties of the cell matrix, in the process of which the hybridization of PBNPs on MCSs was achieved.^{34,35} The PBNPs@MCSs are endowed with antioxidant capacity and photoacoustic imaging functions, while MCSs maintain high viability and differentiation ability. These nanohybridized MCSs integrated three functions on one platform, which is a form of seed cell composition and application. Furthermore, in order to verify the general applicability of this form of seed cells, we used MC3T3-E1 cells, rat bone marrow mesenchymal stem cells (rBMSCs), and human umbilical cord mesenchymal stem cells (hUCMSCs) to conduct a series of experiments.

This study reports the introduction of PBNPs into the process of cell self-organization by nanohybridization. The hybridized MCSs can organically combine nanomedicine and MCSs with a high survival rate, high differentiation starting point, ability to scavenge reactive oxidants, and photoacoustic imaging function. This combination makes the formed spheroids grow in a well-modulated mechanical and inflammatory microenvironment, and the photoacoustic imaging function allows the monitoring of implanted spheroids during recovery and therefore meets multiple clinical needs simultaneously. Through a series of experiments including photoacoustic imaging and in vivo and in vitro antioxidant osteogenesis, we have verified the superior imaging function and in vivo and in vitro antioxidant and bone repair functions of PBNPs@MCSs, which exhibit a great potential for clinical enhancement and treatment applications. Notably, it is not a simple “1 + 1” manner, by performing such “hybridization”, multiple goals including minimizing oxidative stress and free nanoparticles as well as MSC tracing following transplantation are achieved. This study can provide directions and considerations for the subsequent design of nanohybrid active implants.

RESULTS AND DISCUSSION

Characterization of PBNPs and Biomimetic Hydrogels. Size and crystallinity are key factors for the performance of nanomaterials.³⁶ The morphology of PBNPs was observed by transmission electron microscopy (TEM) (Figure S1A) and scanning electron microscopy (SEM) (Figure S1B,C). PVP-coated PBNPs were cubic-shaped with a diameter of ~100 nm, and the particle size was uniform with a “granular” surface, which was due to the presence of the surface coating agent PVP. The unique lattice that dispersed throughout the nanoparticles was observed by high-resolution transmission electron microscopy (HR-TEM) (Figure S1D), and the images clearly showed surface lattice stripes. This indicated the good crystallinity of the PBNPs. The EDX spectrum (Figure S1E) confirmed that the elemental composition of PBNPs was C, N, Fe, and K, with the highest content of Fe elements. The ultraviolet–visible (UV–vis) absorption spectrum (Figure S2A) presented a typical spectrum of PBNPs with a peak at around 700 nm due to the valence charge transfer between Fe(II) and Fe(III). The hydrodynamic sizes of PBNPs were ~131 nm (Figure S2C), and the average zeta potential changes were ~ -21.8 mV, indicating that the PBNP surface was negatively charged (Figure S2B). FTIR spectra (Figure S2D) of the PBNPs displayed a major peak at 2086 cm⁻¹, which is the characteristic peak of $\text{C}\equiv\text{N}$ -stretching from the Fe(II)–CN–Fe(III) bond. The broad peak around 3443 cm⁻¹ can be allocated to the stretching of hydroxyl (O–H), whereas the peak at 1639 cm⁻¹ is from the bending of H–O–H, indicating the presence of interstitial water within PBNPs.

The biomimetic hydrogel preparation method used in this study is based on adjusting the following factors: (1) the ratio of two monomers and (2) the concentration of the cross-linking agent. These factors collectively contribute to the main physical properties of the hydrogel as a cell culture matrix, such as viscoelasticity, Young's modulus, and cell adhesion sites. According to our previous studies, different multicellular structures, such as MCSs, can form through self-organization on hydrogels when Young's modulus, stress relaxation, and/or cell adhesion capacity fall into a certain range, in which the ranges are cell type dependent.^{37,38} In the present study, we

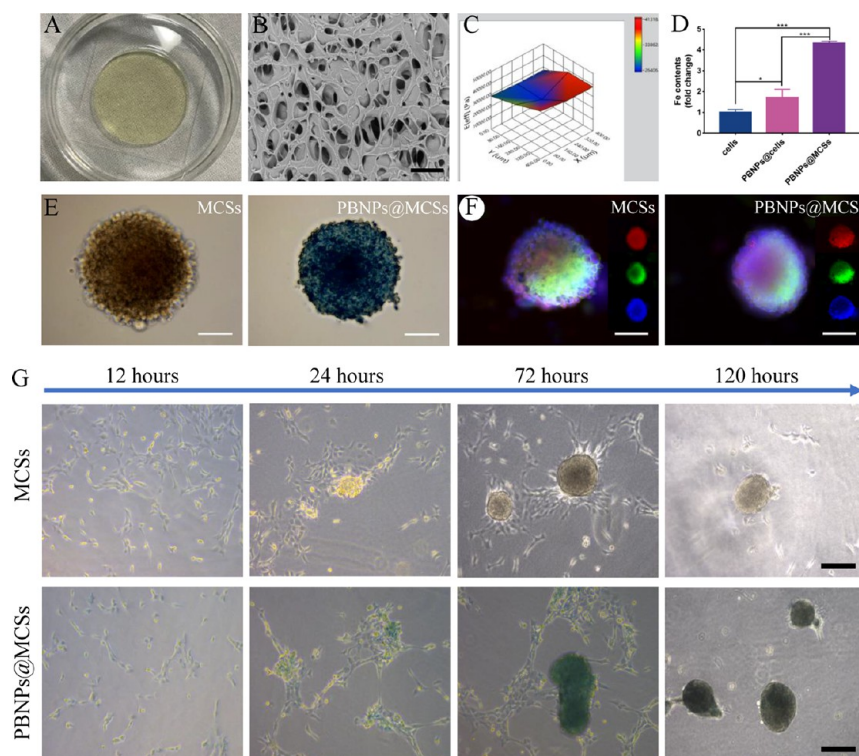
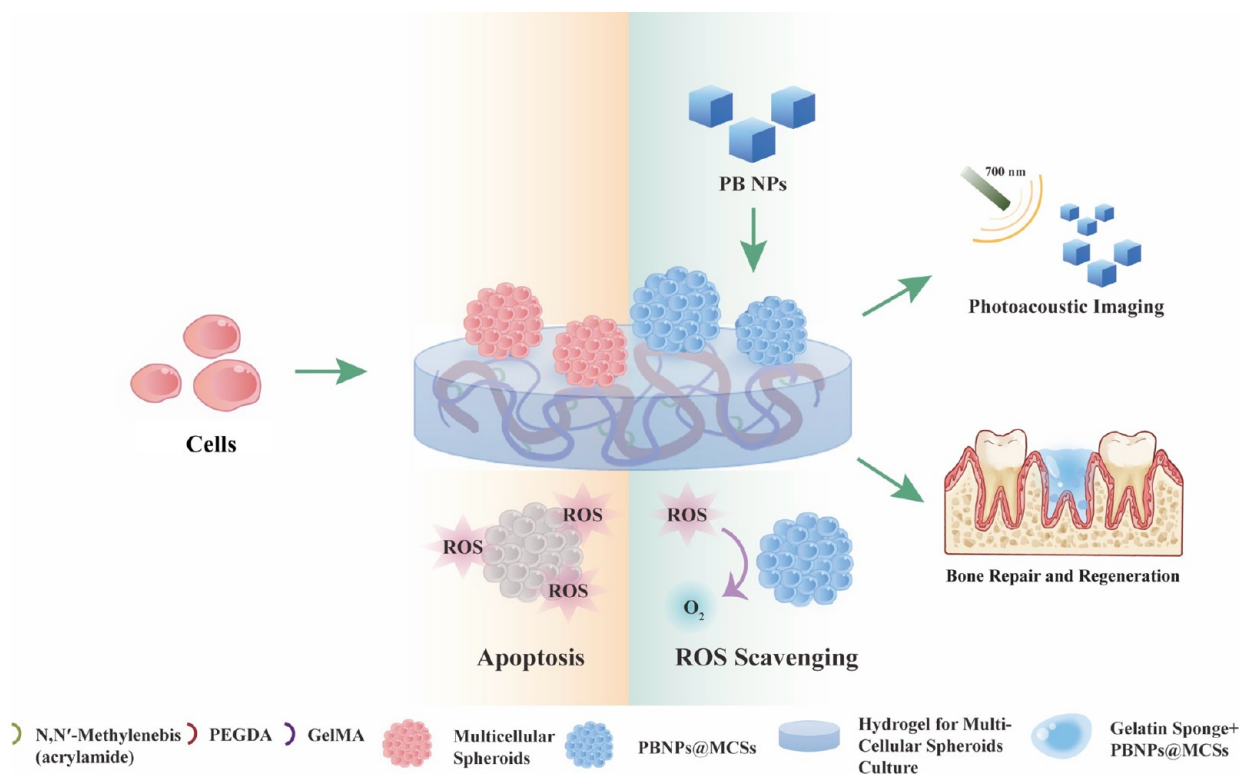


Figure 1. (A) Macroscopic photograph of the biomimetic hydrogel. (B) SEM image of the biomimetic hydrogel. Scale bar = 100 μm . (C) Characterization of the mechanical properties for hydrogels. (D) ICP-MS test of the Fe content. (E) Light microscopy images of MCSs (MC3T3-E1) and PBNPs@MCSs (MC3T3-E1). Scale bar = 100 μm . (F) Immunofluorescence assay of the adhesion factor E-cadherin. Scale bar = 100 μm . (G) Formation of MCSs (MC3T3-E1) cultured on hydrogels for 120 h and the formation of PBNPs@MCSs (MC3T3-E1) cocultured with PBNPs on hydrogels for 120 h. Scale bar = 200 μm .

Scheme 1. Schematic Diagram of Cells and PBNPs Cocultured on the Biomimetic Hydrogel To Form PBNPs@MCSs and Their Application in Photoacoustic Imaging and Antioxidant Proalveolar Bone Regeneration



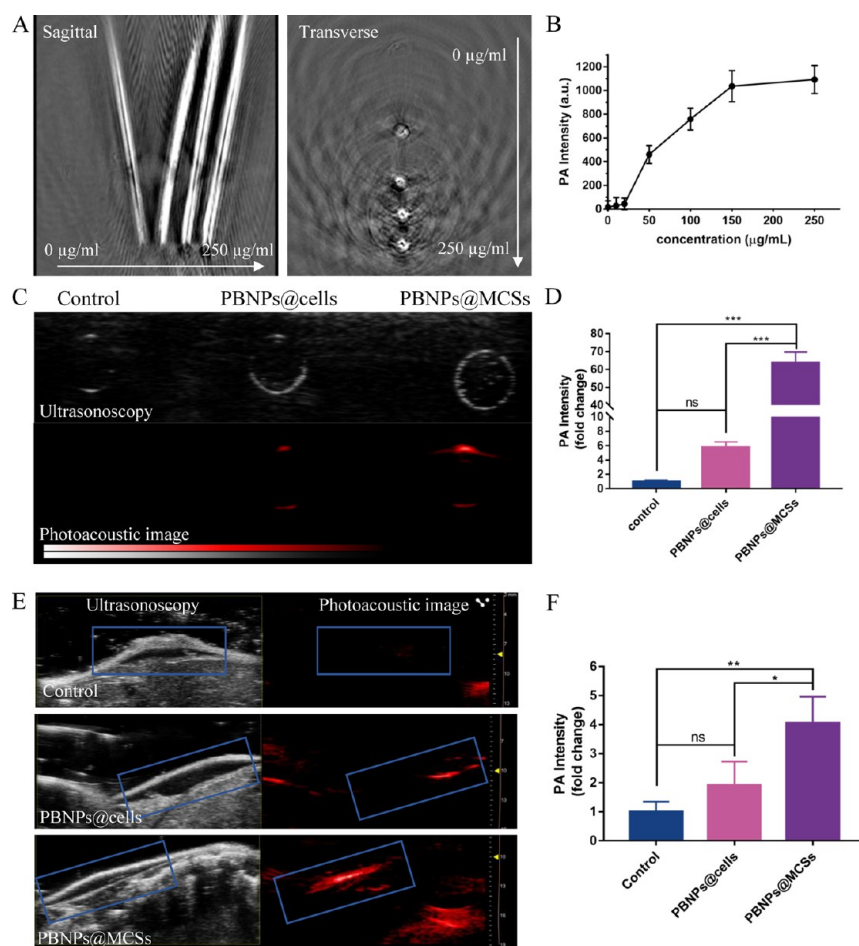


Figure 2. (A) Photoacoustic images of different concentrations of PBNP solutions (from left to right, the concentration increases gradually). (B) Photoacoustic signal intensity of different concentrations of PBNP solutions. (C) Photoacoustic imaging effect of PBNPs@MCSs (MC3T3-E1) at the cellular level. (D) Photoacoustic signal intensity of different groups in picture C (fold change, *** $p < 0.001$, ns represents no significant difference). (E) In vivo photoacoustic imaging of PBNPs@MCSs (MC3T3-E1) after subcutaneous injection in the back of BALB/c mice (left: ultrasound image, right: photoacoustic image). (F) Photoacoustic signal intensity of different groups in picture E (fold change, *** $p < 0.001$, ns represents no significant difference).

developed a hydrogel (Figure 1A) with a porous structure (Figure 1B) for the in vitro culture of MC3T3-E1 cells with surface pores extending into the gel and interconnected. The hydrogels were mechanically homogeneous (Figure 1C), with a Young's modulus of 32.6 ± 6.2 kPa and a half stress relaxation time of 10 ± 4 s. The results showed that the hydrogels were viscoelastic.

Preparation of PBNPs@MCSs. The formation process of PBNPs@MCSs on the hydrogel is shown in Scheme 1. In this study, the mechanical properties of the cell matrix were modulated to induce the self-organization of cells forming MCSs, and during self-organization, the hybridization of the MCSs with PBNPs was achieved. In the hybridized MCSs, PBNPs were present in both intracellular and intercellular spaces (Figures S3 and S4). To determine the predominant form of PBNPs present in the PBNPs@MCSs (MC3T3-E1), ICP-MS experiments were performed, and unlabeled cells that did not form spheroids were set as the control group. The results (Figure 1D) showed that in MCSs (MC3T3-E1), PBNPs were more frequently encapsulated in spheroids, and only a small amount was phagocytosed. Figure 1E shows the structural morphology of MCSs (MC3T3-E1) and PBNPs@MCSs (MC3T3-E1), respectively, both with a diameter of 200 μm and a relatively intact spherical structure. The central part

of the PBNPs@MCSs (MC3T3-E1) was darker than the periphery of the spheroids, which indicated that the encapsulated nanoparticles had good stability in the spheroids. Immunofluorescence staining for the adhesion factor E-cad and phalloidin (Figure 1F) showed that the addition of PBNPs did not significantly alter the expression of cell–cell interaction molecules such as E-cadherin and did not change the overall cytoskeleton and morphology of the MCSs, which exhibited good biocompatibility.

Figure 1G demonstrates the temporal evolution of MC3T3-E1 cells' self-organization into spheroids on hydrogels. After 12 h culture, cell–cell interaction on the hydrogel was initiated by secreting an extracellular matrix, and over the course of 1–5 days of culture, the cells gradually formed multicellular aggregates with improved roundness, which formed separated MCSs after 5 days. Figure S10 shows the MCSs and PBNPs@MCSs of hUCMSCs after 1 and 5 days of incubation on hydrogels. By adjusting the hydrogel parameters, the hUCMSCs could also form spheroids to encapsulate the PBNPs, which have a diameter of about 200 μm .

The formation of nanohybrid MCSs by cell autonomous loading on hydrogels is independent of the internalization of nanoparticles, which on the one hand greatly improves the labeling efficiency of nanoparticles and at the same time can

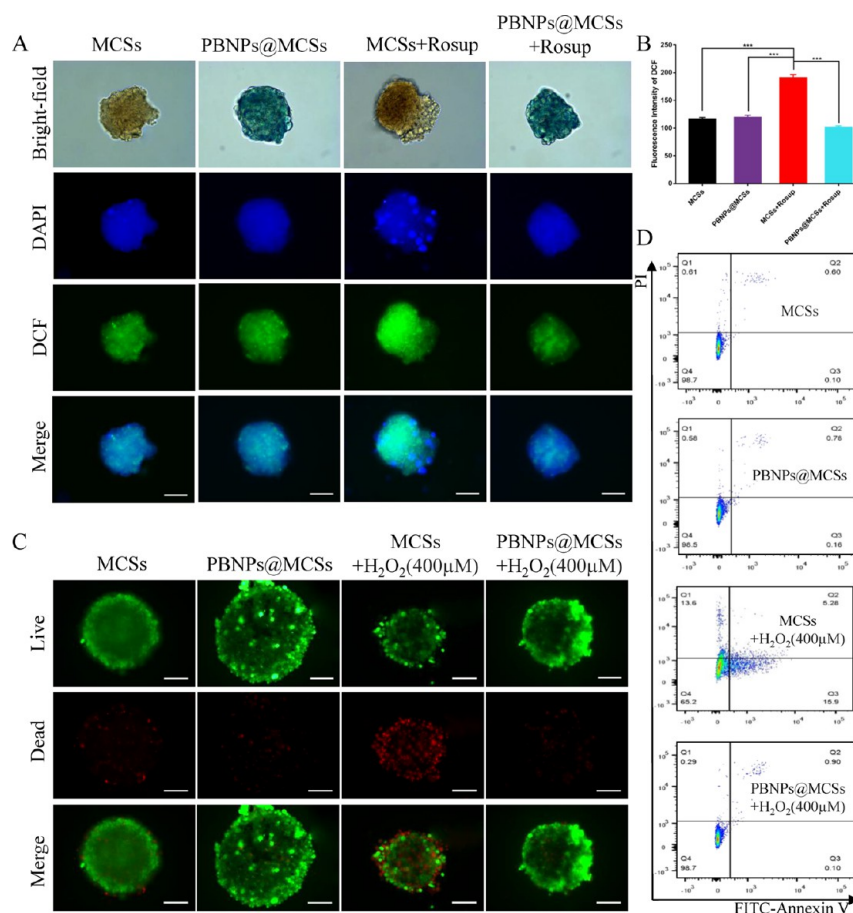


Figure 3. (A) Fluorescence staining images of MCSs (MC3T3-E1) and PBNPs@MCSs (MC3T3-E1) by a DCFH probe. Scale bar = 100 μ m. (B) Quantitation for DCF fluorescence intensity of different groups in picture A (***) $p < 0.001$. (C) Live/dead fluorescence images of MCSs (MC3T3-E1) and PBNPs@MCSs (MC3T3-E1) with or without H₂O₂ treatments. Scale bar = 100 μ m. (D) Antia apoptotic capacity of MCSs (MC3T3-E1) and PBNPs@MCSs (MC3T3-E1) in the peroxidized environment examined by flow cytometry assays.

reduce the damaging effect on cells. On the other hand, this method is more versatile and can label some types of cells and nanoparticles with lower internalization capacity, which makes the function of the nanohybrid MCSs more expansive and provides an application for seed cells for tissue engineering, especially for tissue regeneration in complex microenvironments.

Photoacoustic Imaging of PBNPs@MCSs. PBNPs are an emerging photoacoustic contrast agent with excellent absorption efficiency for NIR laser pulses at wavelengths around 700 nm.²⁹ To investigate whether PBNPs@MCSs (MC3T3-E1) preserved the photoacoustic imaging function of PBNPs, we conducted photoacoustic imaging experiments at three different levels by using NIR laser pulses at 700 nm. First, we examined the photoacoustic imaging effect with different concentrations (0, 10, 20, 50, 100, 150, and 250 μ g/mL) of PBNP solutions (Figure 2A,B), and the results showed that PBNPs could produce strong photoacoustic signals. Among them, PBNPs at a concentration of 50 μ g/mL began to show an obvious photoacoustic imaging effect, and the intensity of the photoacoustic imaging signal increased, depending on the doses of PBNP solutions. Second, at the cellular level, the photoacoustic imaging effect of PBNPs@MCSs (MC3T3-E1) was verified using unlabeled 2D cultured cells as the control group, and cells or MCSs with the same labeling concentration of PBNPs (20 μ g/mL) were imaged, and the photoacoustic signal intensity was recorded (Figure 2C,D). The results

showed that the optical properties of PBNPs were preserved in both 2D and 3D labeling, but the PBNPs@MCSs (MC3T3-E1) showed superior photoacoustic imaging capabilities. Finally, the in vivo photoacoustic imaging of PBNPs@MCSs (MC3T3-E1) was tested by subcutaneous injection into the back of BALB/c mice. The ultrasound image (Figure 2E left) showed a clear hypoechoic cavity, indicating that different groups of cell solutions were successfully injected into the backs of the mice. The photoacoustic images (Figure 2E right) showed the imaging effect of the different groups after injection, and the signal intensity collection results are shown in Figure 2F. In vivo, the PBNPs@MCSs (MC3T3-E1) group still showed better photoacoustic imaging than did the other two groups. These results all suggested that PBNPs@MCSs (MC3T3-E1) had photoacoustic tracer capability to track the location, duration of action, and residual volume of the implant.

Antioxidant Properties of PBNPs@MCSs. Regulating the catalytic activity of nanozymes is significant for their applications in various fields.^{39,40} To verify the antioxidant properties of PBNPs@MCSs (MC3T3-E1), fluorescence staining experiments were first performed using a 2',7'-dichlorodihydrofluorescein diacetate (DCFH-DA) probe to detect the intracellular levels of ROS by the fluorescence of 2',7'-dichlorofluorescein (DCF). Rosup was used in this experiment as a positive control for ROS stimulation. The results (Figure 3A) showed that the DCF fluorescence levels in

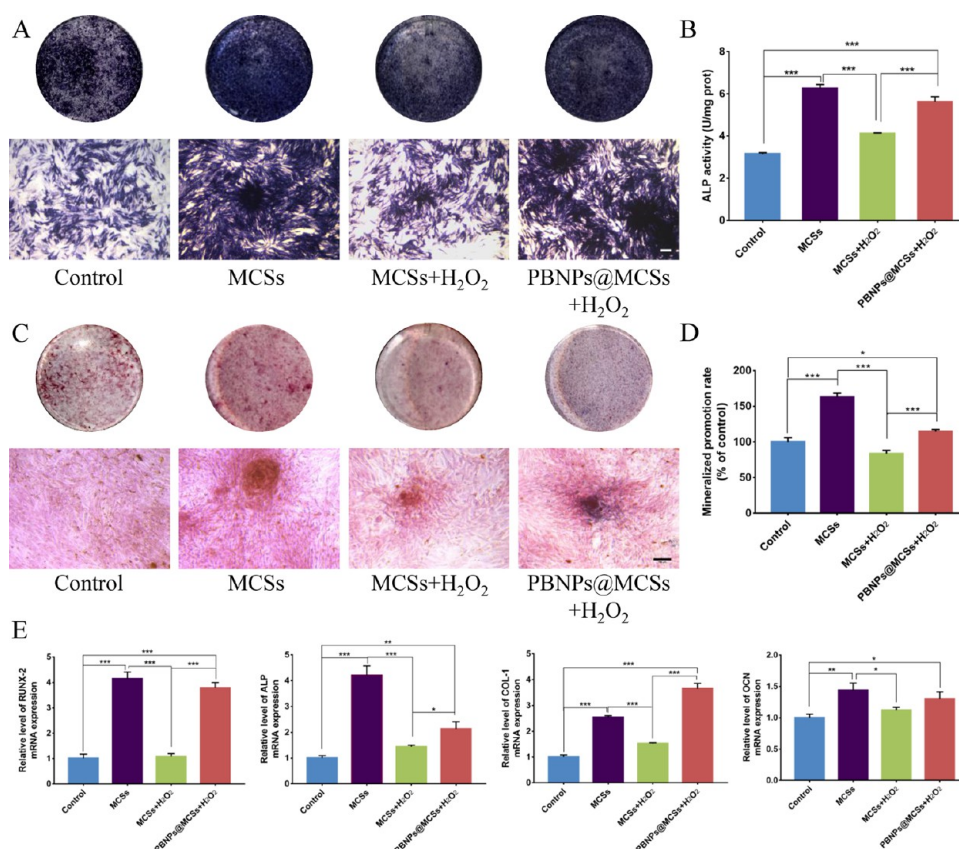


Figure 4. In vitro antioxidant osteogenesis of PBNPs@MCSs (MC3T3-E1). (A) Representative images of ALP staining of 2D cultured cells, MCSs (MC3T3-E1), and PBNPs@MCSs (MC3T3-E1) after osteogenesis induction for 7 days (4 \times). Scale bar = 200 μ m. (B) ALP activity quantitative detection of 2D cultured cells, MCSs (MC3T3-E1), and PBNPs@MCSs (MC3T3-E1) after osteogenesis induction for 7 days ($***p < 0.001$). (C) Representative images of alizarin red staining of 2D cultured cells, MCSs (MC3T3-E1), and PBNPs@MCSs (MC3T3-E1) after osteogenesis induction for 21 days (10 \times). Scale bar = 150 μ m. (D) Semiquantitative detection of calcium nodules of different groups ($*p < 0.05$, $***p < 0.001$). (E) Osteogenic-related gene (RUNX-2, ALP, COL-1, and OCN) mRNA expression levels after osteogenesis induction for 7 days by the qRT-PCR assay ($*p < 0.05$, $**p < 0.01$, $***p < 0.001$).

the PBNPs@MCSs (MC3T3-E1) group were not significantly different from those in the MCSs (MC3T3-E1) group, indicating that PBNPs alone do not enhance the ROS levels in MCSs (MC3T3-E1). The positive control of the MCSs (MC3T3-E1) + Rosup group showed a significant increase in DCF fluorescence levels, while the PBNPs@MCSs (MC3T3-E1) + Rosup group showed a significant decrease in DCF fluorescence levels, suggesting that the addition of PBNPs enhances the antioxidant levels of the MCSs. The quantitative results of DCF fluorescence intensity (Figure 4B) showed consistent results. The mimetic enzymatic activity and scavenging of ROS by PBNPs can be effectively preserved in the hybrid MCSs/PBNPs system.

The degree of antiapoptosis of the MCSs (MC3T3-E1) in the peroxidized environment was further examined using live–dead staining and flow cytometry. The results of the live–dead staining are shown in Figure 3C. There was no significant difference between the live–dead staining results of the PBNPs@MCSs (MC3T3-E1) group and the MCSs (MC3T3-E1) group, indicating that the PBNPs@MCSs (MC3T3-E1) have good biosafety. However, the number of dead cells in the MCSs (MC3T3-E1) was significantly increased under 400 μ M H₂O₂ stimulation, whereas the number of dead cells in the PBNPs@MCSs (MC3T3-E1) was not significantly different from that of the control group. Importantly, under the stimulation of 400 μ M H₂O₂, the

number of nonapoptotic MCSs (Q4) decreased to 65.2% and the number of necrotic MCSs (Q1) increased to 13.6%, while the number of nonapoptotic cells in the PBNPs@MCSs (MC3T3-E1) group under H₂O₂ stimulation was not significantly different from that in the control group (Figure 3D). All these results indicated that PBNPs@MCSs (MC3T3-E1) could enhance the antioxidant properties of cells and protect them from apoptotic necrosis at higher levels of ROS environment.

PBNPs are a type of nanoparticle developed in recent years with multiple enzyme catalytic effects, including peroxidase, catalase, and superoxide dismutase. They can directly act on the lesion site for the treatment of related diseases. Unlike other iron-based nanoenzymes, the multienzyme activity of PBNPs stems from their electron transfer ability, not the Fenton reaction.⁴¹ Studies suggest that the relationship between iron-based nanoparticles and H₂O₂ is generally associated with the Fenton reaction, which produces hydroxyl radicals (\cdot OH) and is a significant contributor to the biotoxicity in the antioxidant process of iron-containing nanoparticles.⁴²

In Vitro Antioxidant Osteogenesis of PBNPs@MCSs. After verifying the antioxidant properties of PBNPs@MCSs (MC3T3-E1), we set out to examine their osteogenic ability in vitro. In the pre-experimental stage, we investigated the effects of different concentrations of PBNPs on the osteogenic

differentiation of MC3T3-E1 cells, and the experimental results, as shown in Figures S5 and S6, showed that the osteogenic differentiation of the MC3T3-E1 cells was not significantly improved with the increase in the concentration of PBNPs under the normal conditions of the medium. The results suggest that PBNPs have no direct promotional effect on osteogenic differentiation of cells. How do PBNPs act on cellular osteogenic differentiation in peroxidative conditions, and can it be accelerating bone regeneration by re-establishing the cellular osteogenic environment just like other materials reported in the articles?^{43–45} Therefore, we added different concentrations of H₂O₂ to the culture medium, and the CCK8 assay was performed to detect the survival rate of the cells, and the results are shown in Figure S7; 200 μ M H₂O₂ could significantly inhibit cell proliferation, and 400 μ M H₂O₂ could directly cause cell apoptosis. In conclusion, we chose to use 200 μ M H₂O₂ to artificially create a cellular peroxidative culture environment to investigate the antioxidant-mediated osteogenesis of PBNPs@MCSs.

After that, MCSs (MC3T3-E1) and PBNPs@MCSs (MC3T3-E1) were seeded to well plates for osteogenesis induction after 5 days of culture on hydrogels, and both the MCSs (MC3T3-E1) and PBNPs@MCSs (MC3T3-E1) were slowly apposed, and the PBNPs in the center of PBNPs@MCSs (MC3T3-E1) could release into the culture medium gradually (Figure S8). After 7 days of osteogenesis induction, ALP staining (Figure 4A) and activity assay (Figure 4B) showed that osteogenesis was significantly inhibited in the MCSs (MC3T3-E1) + H₂O₂ group, while the osteogenic differentiation ability of the PBNPs@MCSs (MC3T3-E1) + H₂O₂ group was recovered close to the level of MCSs (MC3T3-E1) without H₂O₂ treatment. On day 21 of osteogenesis induction, the results of the alizarin red staining (Figure 4C) showed that large red calcium nodules were visible in the MCSs (MC3T3-E1) group with the darkest color, while the MCSs (MC3T3-E1) + H₂O₂ group had the lightest alizarin red staining, and the PBNPs@MCSs (MC3T3-E1) + H₂O₂ group was in between. The semiquantitative results of calcium nodules (Figure 4D) were in general agreement with the alizarin red staining results. In addition, the qRT-PCR results for the expression levels of osteogenic-related genes RUNX-2, ALP, COL-I, and OCN are shown in Figure 4E. The mRNA expression of osteogenic-related genes was significantly suppressed by 200 μ M concentration of H₂O₂ stimulation ($***p < 0.001$), and the mRNA expression levels of osteogenic-related genes in PBNPs@MCSs (MC3T3-E1) were similar to those in the unstimulated MCSs (MC3T3-E1) group. Finally, the expression of RUNX2 protein was observed by immunofluorescence staining for each group at 7 days of osteogenesis induction. RUNX2 was fluorescent in red, the cytoskeleton was fluorescent in green, and the nucleus was fluorescent in blue; the results are shown in Figure 5. The control group was nonspherical cells, and the cells were arranged more regularly. However, the spherical cells seeded on the confocal dish were spread out in all directions and a large quantity of cytoskeletons were overlapped. Under 200 μ M H₂O₂ stimulation, RUNX2+ cells were significantly decreased in the MCSs (MC3T3-E1) + H₂O₂ group, while RUNX2+ cells were not significantly decreased in the PBNPs@MCSs (MC3T3-E1) + H₂O₂ group. The quantitative analysis of the RUNX-2 fluorescence intensity of each group is shown in Figure S9.

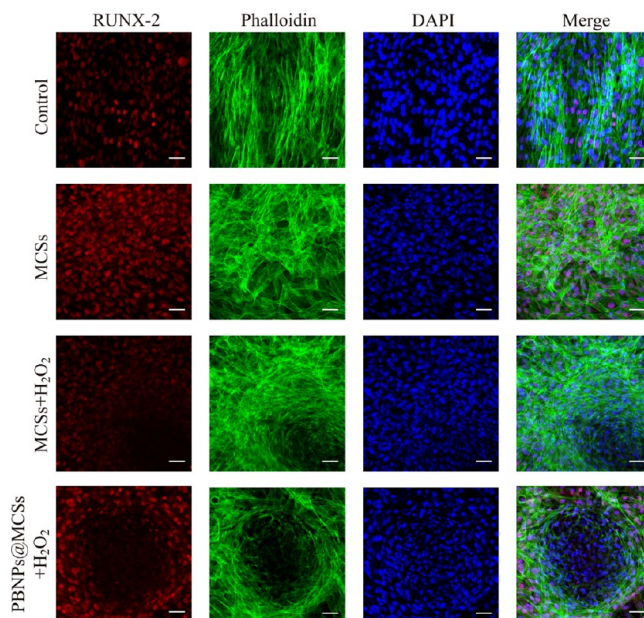


Figure 5. RUNX2 expression of 2D cultured cells (MC3T3-E1), MCSs (MC3T3-E1), and PBNPs@MCSs (MC3T3-E1) with or without H₂O₂ treatments after osteogenic induction for 7 days by immunofluorescence staining. RUNX2 (red), rhodamine phalloidin (green), and DAPI (blue), respectively. Scale bar = 50 μ m.

To further validate the broad applicability of this form of seed cells, we conducted a series of osteogenesis experiments using hUCMSCs, the results of which are shown in Figures S10 and S11. First, we successfully constructed nanohybrid MCSs of hUCMSCs by readjusting the parameters of the biomimetic hydrogel and then validated the in vitro antioxidant contributing bone differentiation function, and the results were consistent with MC3T3-E1 nanohybrid MCSs. That is, PBNPs@MCSs (hUCMSCs) had a stronger osteogenic differentiation ability compared with cells cultured in a 2D environment; in the H₂O₂-stimulated microenvironment, PBNPs@MCSs (hUCMSCs) played a role in regulating the peroxidative microenvironment, and a better osteogenic differentiation effect was obtained compared with the MCSs (hUCMSCs) group.

The above results suggest that, first, formation of MCSs can, to some extent, alter the timeline of osteogenic differentiation of cells. This might be attributed to the absence of an extracellular matrix and physiological relevance of 2D cultured cells, resulting in abnormal metabolism and protein expression, whereas the MCS culture platform can better mimic the in vivo microenvironment, such as complex cell–cell and cell–ECM interactions.^{46,47} Second, PBNPs@MCSs do not alter the biomimetic enzymatic activity of PBNPs. In the peroxidative microenvironment, PBNPs can play a role in mimicking peroxidase activity, on the one hand enhancing the self-antioxidant levels of cells and on the other hand being released into the culture medium to scavenge ROS from the microenvironment. Third, in the nanohybrid MCSs, the release of PBNPs can be gentler and more sustainable, not only for the early stage of osteogenic differentiation but also for the late stage of osteogenic differentiation of cells.

To better demonstrate the protection function of PBNPs to BMSCs, an RNA-seq experiment was conducted to head-to-head compare the responses of BMSC spheroids toward oxidative stress when in the presence or absence of PBNPs. As

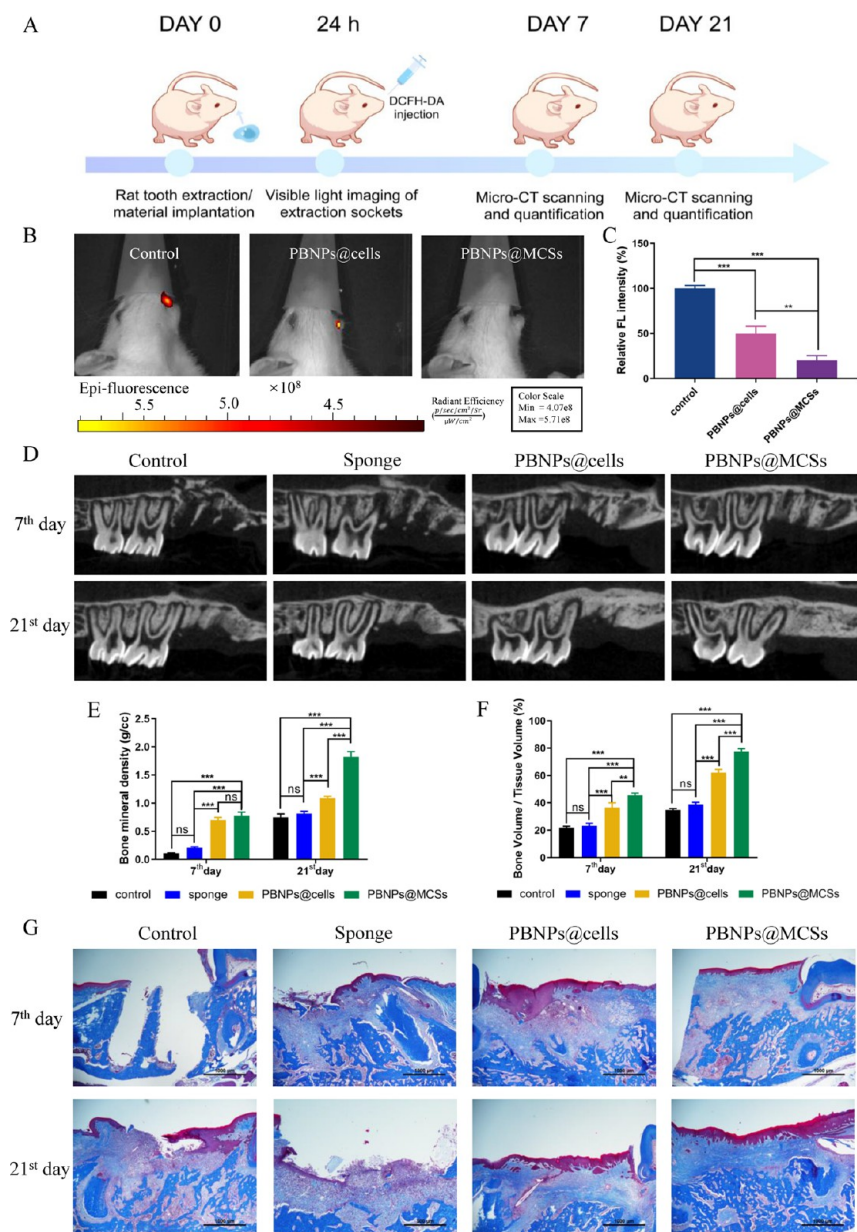


Figure 6. (A) Schematic illustration of in vivo animal experiments. (B) In vivo DCF fluorescence images of extraction sockets after 24 h of surgery captured by a small animal visible light imaging system. (C) Quantitative results of DCF fluorescence intensity (** $p < 0.01$, *** $p < 0.001$). (D) Representative micro-CT sagittal images of maxillary first molars in rats. (E) Results of micro-CT quantitative analysis of BMD (** $p < 0.001$, ns represents no significant difference). (F) Results of micro-CT quantitative analysis of BV/TV (** $p < 0.01$, *** $p < 0.001$, ns represents no significant difference). (G) Representative images of the bone defect specimens that were stained with Masson's trichrome. Black bar: 1 mm.

Figure S12 shows, GSEA pathway enrichment analysis revealed that inflammatory signaling pathways in the PBNPs group (cytokine–cytokine receptor interaction, leukocyte trans-endothelial migration, and toll-like receptor signaling pathway) were significantly downregulated ($NES \leftarrow 1$, $p < 0.05$). These data demonstrate the protection role of PBNPs in ameliorating BMSCs' inflammatory responses toward oxidative stress, which in turn suggests the importance of incorporating PBNPs in the BMSC spheroids during bone repair therapy.

Antioxidant Osteogenesis of PBNPs@MCSs In Vivo. In order to further explore the ability of PBNPs@MCSs in promotion of alveolar bone repair in vivo, we constructed a rat extraction socket bone defect model, and the procedure is shown in Figure S13. Bilateral maxillary first molars were

extracted from rats, and different materials were implanted in the extraction sockets by a randomized control principle and pulled together and sutured. In both the PBNPs@cells group and the PBNPs@MCSs group, gelatin sponges were used as carriers for implantation. In order to provide better biocompatibility of the implant, in the animal experiment part, we used rBMSCs and constructed PBNPs@MCSs (rBMSCs) for the following experiment.

First, to verify that surgical trauma could lead to an increase of ROS levels in the extraction sockets and to test the ability of PBNPs@MCSs (rBMSCs) of ROS scavenging in vivo, DCF fluorescence images were collected and quantified after 24 h of surgery using a small animal visible light imaging system (Figure 6B,C). In the control group, only the extractions were

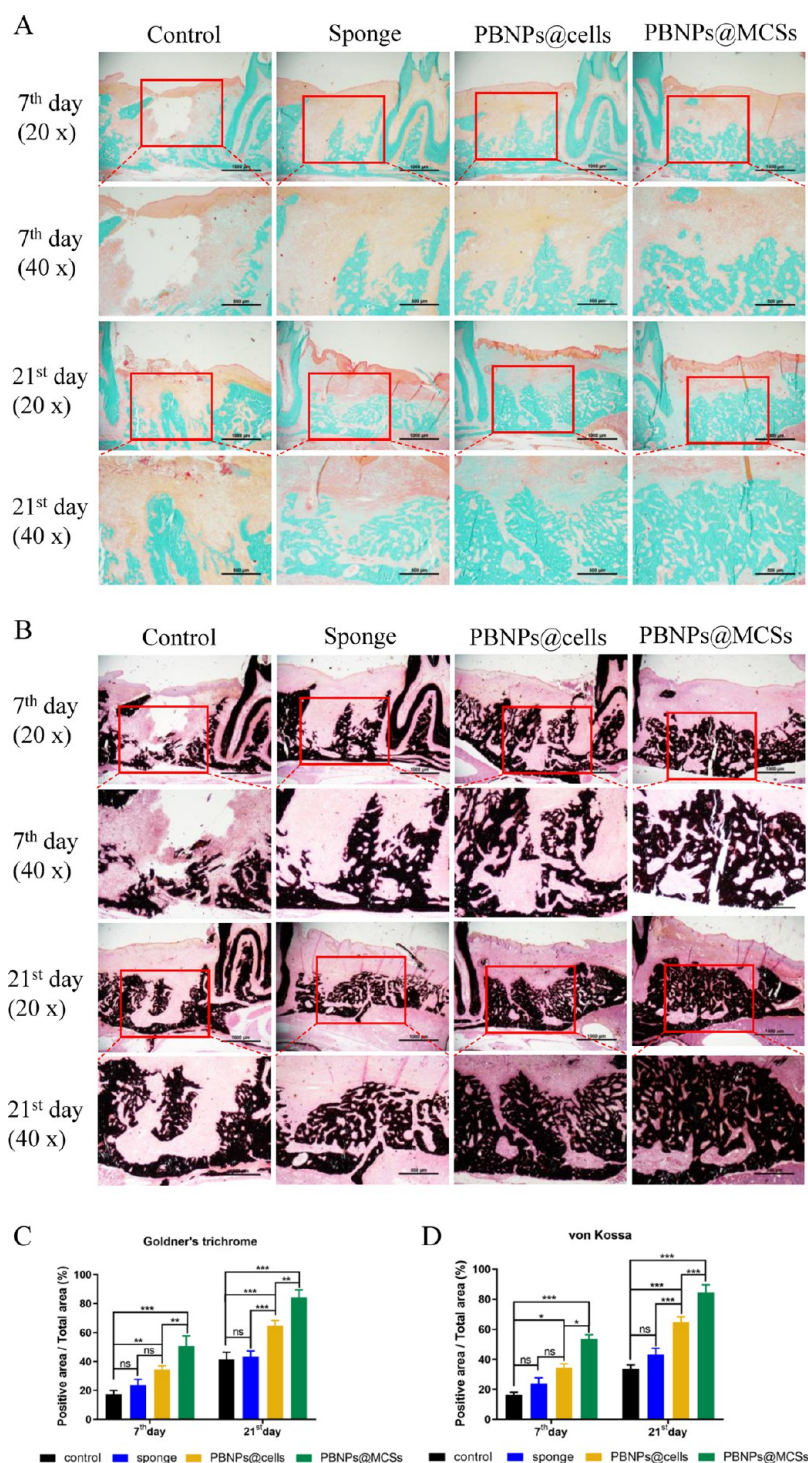


Figure 7. Histological changes in the alveolar bone defect on the 7th day and 21st day after surgery. (A) Representative images of the bone defect specimens that were stained with Goldner's trichrome. Black bar: 1 mm (20 \times) and 0.5 mm (40 \times). (B) Representative images of the bone defect specimens were stained with von Kossa stain. Black bar: 1 mm (20 \times) and 0.5 mm (40 \times). (C) Statistical analysis of the Goldner's trichrome staining results (positive areas/total areas). (D) Statistical analysis of the von Kossa staining results (positive areas/total areas). * $p < 0.05$, ** $p < 0.01$, *** $p < 0.001$, ns represents no significant difference.

performed without any implants. The results showed that ROS levels in the extraction sockets were high at 24 h postoperation, suggesting that the surgical trauma of tooth extraction triggered an increase of ROS in the alveolar sockets.

Representative micro-CT sagittal images of the maxillary first molar fossa on days 7 and 21 after tooth extraction are shown in Figure 6D. At 7 days postoperation, the inter-root

bone compartment in the extraction area had not completely atrophied, and the blank control group still had a large hypodense shadow. In the gelatin sponge group, the edges of the defective area were blurred and a small amount of new bone was formed. The PBNPs@cells (rBMSCs) and PBNPs@MCSs (rBMSCs) groups showed a dotted higher-density shadow with a relatively low bone density and bone volume.

After 21 days of osteogenesis, the inter-root bone compartment had shrunk and disappeared, and there was lamellar new bone production in the alveolar bone defect area in all groups, of which the PBNPs@MCSs (rBMSCs) group had the highest volume and bone density. We further quantified and analyzed the micro-CT images. The results of the bone mineral density (BMD) value analysis (Figure 6E) and the bone volume/total volume (BV/TV) ratio analysis (Figure 6F) both showed no significant difference between the blank control and sponge groups, and the values of the PBNPs@MCSs (rBMSCs) group were significantly higher at the end of each time period compared to those of the control group. Notably, there was no significant difference in new bone density between the PBNPs@cells (rBMSCs) and PBNPs@MCSs (rBMSCs) groups at 7 days, while a significant difference occurred at 21 days, indicating that both the PBNPs@cells (rBMSCs) and PBNPs@MCSs (rBMSCs) groups were able to exert antioxidant properties in the alveolar sockets. This could be because the cells in the PBNPs@cells (rBMSCs) group were more dispersed so that their survival rate and duration of action were lower, whereas the spheroids in the PBNPs@MCSs (rBMSCs) group were tightly connected and could survive longer in a complex oral microenvironment, allowing for a more sustained release of nanodrugs, regulating redox homeostasis, decreasing ROS levels, reducing inflammation, and finally promoting bone repair.

Then, alveolar bone defect specimens were stained with Masson's trichrome (Figure 6G), Goldner's trichrome (Figure 7A), and von Kossa stain (Figure 7B). There was better formation and mineralization of new bone in the PBNPs@MCSs (rBMSCs) group. Histomorphometric analysis showed that the PBNPs@MCSs (rBMSCs) group had a significantly higher volume of mineralized bone and positively stained collagen (Figures S14 and 7C,D). Taken together, these results are indicative of the *in situ* bone regeneration potential of PBNPs@MCSs.

At last, to verify the biosafety of PBNPs *in vivo*, H&E staining was performed on the major organs of the sponge, PBNPs@cells (rBMSCs), and PBNPs@MCSs (rBMSCs) groups at 21 days after alveolar socket implantation. The results (Figure S15) showed no significant morphological changes or signs of inflammation in the tissues of the organs. Analysis of serum levels of glutamate transaminase (ALT), aspartate transaminase (AST), and alkaline phosphatase (ALP) in all groups of rats showed that all parameters were within the normal reference range (Figure S16). These results indicated that at a dose of 20 $\mu\text{g/mL}$, the systemic toxicity of PBNPs was negligible.

In summary, single-function cell implants are no longer sufficient to meet the demand for tissue engineering of seed cells. Bone defects caused by tooth extraction can largely heal on their own; however, tooth extraction not only reduces the width and height of the alveolar ridge but also leads to compensatory filling at the extraction site. Although immediate implantation techniques have matured, limitations in implant morphology mean that immediate implantation is not feasible for multirooted teeth in the posterior region. Furthermore, due to the complexity of the oral microenvironment and the high incidence of inflammation, cells often struggle to survive post-transplantation. In this study, the mechanically tunable biomimetic hydrogel was used to modulate the mechanical properties of the cell matrix to guide cells to self-organize into MCSs, in the process achieving hybridization of PBNPs to

MCSs. This work provides a relatively simple and convenient method for constructing these hybrid MCSs, emphasizing the rapid operability of the process. This is a particular form of seed cell composition, and we have validated the broad applicability of this form of seed cells, which can be applied to various types of cells such as MC3T3-E1 cells, hUMSCs, and rBMSCs. The previous studies loaded cells with nanodrugs and released them by cytosolic action or used surface modification methods to target drug release, and these delivery methods were often of insufficient efficiency.^{29,48–50} The application of a nanohybrid approach effectively improves the delivery efficiency of nanodrugs that could be sustained for a long duration of action. Our design rationally combines the advantages of MCSs and nanoparticles, and therefore, we constructed a multifunctional composite implant that integrates imaging, microenvironmental modulation, and antioxidation for bone repair. Our intention is to provide an application form for seed cells in tissue engineering through this approach. After the mechanisms are fully elucidated, we can further test the proalveolar bone repair effect in large animals and eventually realize the dental clinical application of PBNPs@MCSs.

CONCLUSIONS

We provide a form of nanozyme application on a form of seed cell composition by means of nanohybridization, in which PBNPs are loaded during cellular self-organization into spheroids. The nanohybridized MCSs were biocompatible and preserved the mimetic enzymatic activity of PBNPs, which can act as a microenvironmental regulator to continuously enzymatically dissolve ROS in the hypoxic microenvironment of the bone defect area of the extraction socket. With these settings, the hybridized MCSs generated oxygen, maintained redox homeostasis in the bone defect area, reduced the development of inflammation, and promoted bone repair. The hybridized MCSs also preserved the photoacoustic imaging function of PBNPs, allowing early diagnosis and tracing of implants, which is important for wound healing around the implants. In summary, the PBNPs@MCSs composite implant designed in this study combined photoacoustic imaging, microenvironmental modulation, and antioxidant bone repair. It can be used as a form of tissue engineering seed cell application and nanodrug delivery, which is expected to provide a treatment strategy for patients with alveolar bone resorption and also demonstrate the application of nanodrugs in the field of tissue engineering.

MATERIALS AND METHODS

Preparation of GelMA/PEGDA Composite Biomimetic Hydrogels. Poly(ethylene glycol) diacrylate (PEGDA) (50 mg), *N,N'*-methylenebis(acrylamide) (0.2 wt %), and gelatin methacryloyl (GelMA) (20 mg) were added to 1 mL of water and dissolved at 50 °C for 1 h. Lithium phenyl (2,4,6-trimethylbenzoyl) phosphinate (LAP) (5 mg) was added and dissolved for 5 min. The above solution was then poured into a custom-made cylindrical mold (inner diameter: 30 mm; thickness: 1 mm) and exposed to visible light (405 nm) for 15 s. The prepared composite hydrogels were rinsed with ultrapure water, soaked for 3 days, and transferred into 12-well plates. After sterilization with ethylene oxide, the hydrogels were used as cell culture substrates.

Characterization of Biomimetic Hydrogels. After the hydrogels were lyophilized, the internal porous structure of the hydrogels was photographed by using SEM. Young's modulus and stress relaxation of the bionic hydrogels were determined using a Piuma

nanoindenter. The nanoindenter optical probe was spherical with a stiffness of 3.54 N m^{-1} and a tip radius of $54 \mu\text{m}$. To measure Young's modulus, the probe was set to indent $10 \mu\text{m}$ in 2 s and unloaded after 1 s of resting. To measure stress relaxation, the probe was set to indent $15 \mu\text{m}$ in 5 s, held for 600 s, and then unloaded.

Formation and Culture of MCSs. After aspirating the sterilized hydrogel, the plate was rinsed three times with PBS, 1 mL of PBS was added to each well, and the mixture was placed in a 37°C , 5% CO_2 incubator for 24 h. After aspirating the PBS, 1 mL of α -MEM complete medium (containing 10% FBS) was added to each well and precultured in a 37°C , 5% CO_2 incubator for 24 h. The medium was removed and MC3T3-E1 cells were inoculated on a 12-well plate at a density of 150,000/well, where the PBNPs@MCSs (MC3T3-E1) group was added with $20 \mu\text{g/mL}$ of PBNP solution and placed in a cell culture incubator for observation. Five days later, MCSs were taken for subsequent experiments. PBNPs@MCSs (hUCMSCs) and PBNPs@MCSs (rBMSCs) were formed in a manner consistent with MC3T3-E1 cells in the DMEM (containing 10% fetal bovine serum, 100 U/mL penicillin, and $100 \mu\text{g/mL}$ streptomycin), and cells were inoculated at a density of 100,000/well.

ICP-MS Assay. MC3T3-E1 cells cocultured with $20 \mu\text{g/mL}$ PBNPs for 5 days were collected, and the Fe element content of different groups was determined by inductively coupled plasma mass spectrometry (ICP-MS) to analyze the amount of PBNPs entering into the cytoplasm and being encapsulated in the MCSs. There were three groups: control group (cells), PBNPs@cells (PBNPs-labeled 2D cultured cells) group, and PBNPs@MCSs (MC3T3-E1) group. Samples were all digested and fixed to 10 mL for determination.

Immunofluorescence Staining of Adhesion Proteins. The MCSs (MC3T3-E1) and PBNPs@MCSs (MC3T3-E1) after 5 days of culture on gels were fixed in 4% paraformaldehyde for 30 min at 4°C , washed twice with PBST, and incubated with an immunofluorescent blocking solution for 10 min at room temperature. The corresponding secondary antibody (1:200) was added and incubated for 1 h at room temperature, protected from light, and washed 3 times with PBST. Then, phalloidin stain (1:400) was added and incubated for 20 min at room temperature, washed 3 times with PBST, finally stained with DAPI (1:1000) for 5 min at room temperature, washed with PBS, and observed with an automatic inverted fluorescence microscope.

Photoacoustic Imaging Experiments. Different concentrations of PBNP solutions: different concentrations of PBNP solutions were prepared using pure water at 0, 10, 20, 50, 100, 150, and $250 \mu\text{g/mL}$. The sample solutions to be tested were added to the test tubes of the photoacoustic imaging equipment and photographed on the machine; photoacoustic images were acquired and the photoacoustic signal intensities of the different concentrations of solutions were recorded.

At the cellular level: unlabeled 2D cultured cells (MC3T3-E1) and PBNPs@cells (MC3T3-E1) were used as the control group, and PBNPs@cells (MC3T3-E1) and PBNPs@MCSs (MC3T3-E1) were labeled with $20 \mu\text{g/mL}$ PBNPs. Cell precipitates from different groups were collected and added to the agarose gel model. The samples were placed in a photoacoustic imaging system to observe the photoacoustic imaging capability and to acquire images, while the photoacoustic signal intensities of different sample groups were recorded and analyzed.

Subcutaneous injection in mice: PBNPs@cells (MC3T3-E1) and PBNPs@MCSs (MC3T3-E1) were prepared in advance, and $100 \mu\text{L}$ of the cell suspension was injected subcutaneously in the back of BALB/c mice, respectively; then, photoacoustic imaging and signal intensity acquisition were immediately carried out.

Antioxidant Properties of MCSs. Following the steps of the ROS kit instructions, MC3T3-E1 cells were labeled with the DCFH-DA fluorescent probe, and the ROS levels of MCSs were observed by inverted fluorescent microscopy. The cells were divided into the following groups: MCSs (MC3T3-E1) group, PBNPs@MCSs (MC3T3-E1) group, MCSs (MC3T3-E1) + Rosup group, and PBNPs@MCSs (MC3T3-E1) + Rosup group. The DCFH-DA probe was diluted with the serum-free medium to a final concentration of 20 nmol/L and incubated with cells for 20 min at 37°C , mixing upside

down every 3–5 min intervals. Twenty minutes later, the cells were washed three times with the serum-free medium to fully remove DCFH-DA that had not entered the cells. In addition, the MCSs (MC3T3-E1) + Rosup group and the PBNPs@MCSs (MC3T3-E1) + Rosup group were treated with the Rosup reagent for 15 min at 37°C ($10 \mu\text{L}$ of Rosup per 1 mL of medium) and washed three times with the serum-free medium before adding the probes. Drops of MCSs (MC3T3-E1) and PBNPs@MCSs (MC3T3-E1) loaded with probes were added to cell slides, and the fluorescence intensity was observed by a fully automated inverted fluorescence microscope.

Live–Dead Staining and Flow Cytometric Analysis. The cells were divided into the following groups: MCSs (MC3T3-E1) group, PBNPs@MCSs (MC3T3-E1) group, MCSs (MC3T3-E1) + H_2O_2 group, and PBNPs@MCSs (MC3T3-E1) + H_2O_2 group. MCSs (MC3T3-E1) and PBNPs@MCSs (MC3T3-E1) cultured on gels for 5 days were taken and stimulated by a $400 \mu\text{M}$ concentration of H_2O_2 for 4 h and then washed 3 times with PBS. Staining was performed according to the operating manual of the live–dead staining kit, and groups of live and dead cells were observed under an inverted fluorescent microscope. For flow apoptosis experiments, fluorescein (FITC, Alexa Fluor488, etc.)-labeled Annexin-V and propidium iodide (PI) were used as probes, and the MCSs (MC3T3-E1) and PBNPs@MCSs (MC3T3-E1) were examined by flow cytometry.

ALP Staining and ALP Activity Assay. MCSs (MC3T3-E1) and PBNPs@MCSs (MC3T3-E1) cultured on the gels for 5 days were collected and inoculated in a new 12-well plate at a density of 50,000/well. After they had fused to 60–70%, the original medium was removed, the MC3T3-E1 osteogenic induction medium was added, and the solution was changed every 2–3 days. The nonosteogenic MC3T3-E1 cells were used as the control group and divided into 4 groups: control group, MCSs (MC3T3-E1) group, MCSs (MC3T3-E1) + H_2O_2 group, and PBNPs@MCSs (MC3T3-E1) + H_2O_2 group. Among them, the H_2O_2 + MCSs (MC3T3-E1) group and the H_2O_2 + PBNPs@MCSs (MC3T3-E1) group were readed with H_2O_2 solution at a final concentration of $200 \mu\text{mol/L}$ at each change of induction solution. The osteogenic induction medium for PBNPs@MCSs (hUCMSCs) was a complete medium supplemented with 10 nM dexamethasone, 10 mM sodium β -glycerophosphate, and $50 \mu\text{g/mL}$ of ascorbic acid, and the stimulating concentration of H_2O_2 solution was $50 \mu\text{M}$. Osteogenesis of PBNPs@MCSs (rBMSCs) was induced by the rBMSC culture solution.

After 7 days of osteogenic induction, the old culture medium was aspirated and discarded. Then, 1 mL of 4% paraformaldehyde was added to each well and fixed at room temperature for 30 min. After 3 gentle washes with PBS, 1 mL of freshly prepared BCIP/NBT staining solution was added to each well, stained at room temperature, and protected from light until color development. Then, $100 \mu\text{L}$ of Western and IP cell lysate was added to each well, lysed on ice for 1–2 s, and blown with a gun several times to bring the lysate into full contact with the cells. After sufficient lysis, the mixture was centrifuged at $14,000 \text{ g}$ for 5 min, and the supernatant was removed for the ALP activity assay. After the chromogenic substrate solution and standard working solution were prepared according to the kit instructions, 96-well plates were set up with blank control wells, standard wells, and sample wells, and different amounts of assay buffer, chromogenic substrate, sample, or standard working solution were added, gently tapped and mixed, and incubated at 37°C for 10 min; then, $100 \mu\text{L}$ of reaction termination solution was added to each well to terminate the reaction, and the absorbance was measured at 405 nm using an enzyme marker. The absorbance was measured at 405 nm using an enzyme marker. The alkaline phosphatase activity was calculated according to the formula in the instructions. The protein concentrations of the different samples were determined by using the BCA protein concentration assay kit. Finally, the ALP activity of each group was calculated from the alkaline phosphatase activity and protein concentration.

Alizarin Red Staining and Semiquantification. Cells grouping and osteogenic induction were performed as described above. After 21 days of osteogenic induction, the original culture medium was aspirated and discarded, and the cells were fixed with 4%

paraformaldehyde at room temperature for 30 min. The fixative was removed, and the cells were gently washed with ultrapure water and stained with alizarin red S staining solution for ARS. After incubation for 5 min at room temperature, the staining solution was aspirated, and the cells were gently washed 3 times with ddH₂O. The calcium nodule staining was observed under the scanner and inverted light microscope and photographed. The stained cells were then immersed in 10% (w/v) cetylpyridinium chloride and gently shaken on a shaker for 1 h. After the calcium nodules were fully dissolved, the absorbance values at 550 nm were measured by a microplate spectrophotometer to further quantify calcium mineralization.

Quantitative Reverse Transcription-Polymerase Chain Reaction. Cells were collected at 7 days of osteogenic differentiation by digestion with 0.25% trypsin and centrifuged at 1000 rpm for 5 min. Total RNA was extracted from the cells using the TIANGEN Total RNA Extraction Kit according to the instructions, and the RNA concentration was determined by a UV spectrophotometer. A reverse transcription system was prepared with 500 ng of RNA, and the RNA was reverse transcribed to cDNA in the amplifier. Then, 10 μ L of the PCR reaction system was prepared, added sequentially to a 384-well plate, mixed, centrifuged, and amplified on a real-time quantitative fluorescence PCR instrument. Using β -actin as an internal reference, the primer sequences for the osteogenesis-related genes of MC3T3-E1 cells and hUCMSCs are shown in Tables S1 and S2 in the Supporting Information, respectively. The relative expression of osteogenic genes in each group of cells was calculated using the $2^{-\Delta\Delta CT}$ method.

Immunofluorescence Staining for RUNX2 Protein. The MCSs (MC3T3-E1) were inoculated, spread, and fused to about 60–70%; the original medium was removed, the osteogenic induction medium was added, and the medium was changed every 2–3 days. After 7 days of osteogenic induction, the expression of Runx-2 in each group of cells was detected by immunofluorescent staining. Cells were fixed in 4% paraformaldehyde for 30 min at 4 °C, washed twice with PBST, and an immunofluorescence blocking solution was added and permeabilized for 10 min at room temperature. A freshly prepared Runx-2 primary antibody solution (1:400) was added and incubated overnight at 4 °C. After washing 3 times with PBST, the Alexa Fluor 594-conjugated secondary antibody (1:200) was added and incubated for 1 h at room temperature, protected from light, and washed 3 times with PBST. Then, a ghost pencil cyclic peptide staining solution (1:400) was added and incubated for 20 min at room temperature, washed 3 times with PBST, stained with DAPI (1:1000) for 5 min at room temperature, and washed with PBS; then, the fluorescence image was observed with a laser confocal microscope and photographs were taken.

Animal Experiments. The animals used in this experiment were 5-week-old SPF-grade male SD rats, housed in the Medical Laboratory Animal Centre, and the experiment was approved by the Experimental Animal Welfare Ethics Committee of Nanjing Medical University (IACUC-2304002).

Establishment of the Rat Tooth Extraction Model and Material Implantation. To further verify the osteogenesis-promoting effect of PBNPs@MCSs (rBMSCs), in vivo experiments were performed in rats. The experiment was divided into four groups: blank control group (no material was placed), gelatin sponge group, gelatin sponge + PBNPs@cells (rBMSCs) group (PBNPs-labeled nonspherical cells), and gelatin sponge + PBNPs@MCSs (rBMSCs) group.

Each rat was extracted from bilateral maxillary first molar tissue under general anesthesia. The extraction sockets with broken roots were discarded, and the experiment was carried out using the randomized control principle. The implant material was prepared in advance: PBNPs@cells (rBMSCs) and PBNPs@MCSs (rBMSCs) were collected, the concentration was adjusted to 2×10^7 /mL, and the cell suspension was inoculated with absorbable gelatin sponges (approximately 2 mm in length and width) to a “supersaturated” state. The prepared material should be placed in the extraction socket as soon as possible. The soft tissues were pulled together and sutured for further feeding.

Visible Light Imaging of Extraction Sockets. To observe the inhibitory effect of PBNPs on ROS levels in extraction sockets, 24 h after molding, DCFH-DA probes were injected into the extraction wounds of rats, and visible light imaging was performed on a small animal imaging system to detect ROS levels at the molding site. The group without any material placed was used as the control, and the gelatin sponge + PBNPs@cells (rBMSCs) group and the gelatin sponge + PBNPs@MCSs (rBMSCs) group were used as the test groups.

Micro-CT Scans and Quantitative Analysis. The jaws of rats with 1 and 3 weeks of osteogenesis were scanned separately using micro-CT to observe tissue regeneration in the alveolar bone defect area. The scanning parameters were as follows: scanning voltage, 55 kVp; current, 72 μ A; resolution, 15.6 μ m. 3D reconstruction and quantitative analysis of the acquired images were performed using a CT analyzer, CTvox, and DataViewer software.

Histological Staining. Osteogenic 1- and 3-week rat jaw bone samples were fixed in 4% paraformaldehyde. After dehydration using an ascending series of ethanol, the specimens were infiltrated with purified methyl methacrylate and polymerized. The nondecalcified specimens were sectioned longitudinally at a thickness of ~ 50 μ m. The sections were stained with Goldner's trichrome, von Kossa, and Masson's trichrome. For Goldner's trichrome, green areas (indicative of mineralized bone) in the region of interest were considered positive. For von Kossa staining, dark brown areas (indicative of calcified nodules) were considered positive. For Masson's trichrome, blue areas (indicative of collagen fibrils) were considered positive. The positive area fractions (positive areas/total areas, PA/TA) were measured by using ImageJ software (National Institute of Health, Bethesda, MD, USA) and analyzed.

Long-Term Toxicity Test. The PBNPs@cells (rBMSCs) and PBNPs@MCSs (rBMSCs) groups were used as the test groups and rats without any material were used as the control group. Three weeks later, the rats were executed and major organs (heart, liver, spleen, lungs, and kidneys) were collected as tissue samples. Tissue samples were fixed in 4% paraformaldehyde, paraffin embedded, sectioned, and stained with H&E. Blood was collected and serum was separated by cardiac blood sampling. The results were analyzed.

Statistical Methods. All data were expressed as mean \pm standard deviation ($\bar{x} \pm s$), and GraphPad Prism 7 was used for graphing. Statistical analysis was performed using Student's *t* test between two groups and two-way ANOVA for more than two groups. The least-significant difference (LSD) method was used to compare two groups, and a *p* value < 0.05 was considered statistically significant (**p* < 0.05 , ***p* < 0.01 , ****p* < 0.001).

ASSOCIATED CONTENT

Supporting Information

The Supporting Information is available free of charge at <https://pubs.acs.org/doi/10.1021/acsnano.3c06835>.

Characterization of PBNPs; ALP staining; CCK-8 assay result; quantitation for RUNX-2 fluorescence intensity; representative light microscopy images of MCSs and PBNPs@MCSs; PBNPs internalize into single cells and hybridize with MCSs; in vitro antioxidant osteogenesis of PBNPs@MCSs; procedure of establishment of a rat extraction socket bone defect model and implantation of materials; statistical analysis of the Masson's trichrome staining results; H&E staining of major organs; and osteogenic-related gene primer sequences of qPCR (MC3T3-E1 and hUCMSCs) (PDF)

AUTHOR INFORMATION

Corresponding Authors

Ke Hu — School of Biomedical Engineering and Informatics, Department of Biomedical Engineering, Nanjing Medical

University, Nanjing 211166 Jiangsu, China; Email: kehu@njmu.edu.cn

Feimin Zhang – Department of Prosthodontics, Jiangsu Province Key Laboratory of Oral Diseases, Jiangsu Province Engineering Research Center of Stomatological Translational Medicine, Nanjing Medical University, Nanjing 210029 Jiangsu, China; orcid.org/0000-0003-3833-8923; Email: fmzhang@njmu.edu.cn

Authors

Lu Chen – Department of Prosthodontics, Jiangsu Province Key Laboratory of Oral Diseases, Jiangsu Province Engineering Research Center of Stomatological Translational Medicine, Nanjing Medical University, Nanjing 210029 Jiangsu, China; Shaoxing Stomatological Hospital, Shaoxing 312000 Zhejiang, China

Shijia Tang – Department of Prosthodontics, Jiangsu Province Key Laboratory of Oral Diseases, Jiangsu Province Engineering Research Center of Stomatological Translational Medicine, Nanjing Medical University, Nanjing 210029 Jiangsu, China

Jiamin Zhang – School of Biomedical Engineering and Informatics, Department of Biomedical Engineering, Nanjing Medical University, Nanjing 211166 Jiangsu, China

Caiying Zhong – School of Biomedical Engineering and Informatics, Department of Biomedical Engineering, Nanjing Medical University, Nanjing 211166 Jiangsu, China

Xueqin Xu – Nanjing Stomatological Hospital, Affiliated Hospital of Medical School, Nanjing University, Nanjing 210000, China

Jia Yan – Department of Prosthodontics, Jiangsu Province Key Laboratory of Oral Diseases, Jiangsu Province Engineering Research Center of Stomatological Translational Medicine, Nanjing Medical University, Nanjing 210029 Jiangsu, China

Zhaobin Guo – Institute of Interdisciplinary Integrative Medicine Research, Shanghai University of Traditional Chinese Medicine, Shanghai 201203, China

Complete contact information is available at: <https://pubs.acs.org/10.1021/acsnano.3c06835>

Author Contributions

L.C.: acquisition of data, analysis and interpretation of data, drafting or revising the article; S.T.: analysis and interpretation of data; J.Z.: acquisition of data and analysis and interpretation of data; C.Z., X.X., and J.Y.: acquisition of data; Z.G.: drafting or revising the article; K.H.: conception and design, acquisition of data, analysis and interpretation of data, provision of funding; F.Z.: conception and design, provision of funding, supervision. L.C., S.T., and J.Z. contributed equally to this work.

Notes

The authors declare no competing financial interest.

ACKNOWLEDGMENTS

This work was supported by the National Key Research and Development Program of China (2021YFA1201302/2021YFA1201301), the Priority Academic Program Development of Jiangsu Higher Education Institution (PADA, 2018-87), and the Youth Science Foundation Project of China (82304446).

REFERENCES

- (1) Kinane, D. F.; Stathopoulou, P. G.; Papapanou, P. N. Periodontal Diseases. *Nat. Rev. Dis. Primers* **2017**, *3*, 17038.
- (2) Peres, M. A.; Macpherson, L. M. D.; Weyant, R. J.; Daly, B.; Venturelli, R.; Mathur, M. R.; Listl, S.; Celeste, R. K.; Guarnizo-Herreño, C. C.; Kearns, C.; Benzian, H.; Allison, P.; Watt, R. G. Oral Diseases: A Global Public Health Challenge. *Lancet* **2019**, *394* (10194), 249–260.
- (3) Huang, X.; Xie, M.; Xie, Y.; Mei, F.; Lu, X.; Li, X.; Chen, L. The Roles of Osteocytes in Alveolar Bone Destruction in Periodontitis. *J. Transl. Med.* **2020**, *18* (1), 479.
- (4) Araújo, M. G.; Silva, C. O.; Souza, A. B.; Sukekava, F. Socket Healing with and without Immediate Implant Placement. *Periodontol* **2019**, *79* (1), 168–177.
- (5) Boda, S. K.; Almoshari, Y.; Wang, H.; Wang, X.; Reinhardt, R. A.; Duan, B.; Wang, D.; Xie, J. Mineralized Nanofiber Segments Coupled with Calcium-Binding BMP-2 Peptides for Alveolar Bone Regeneration. *Acta Biomater* **2019**, *85*, 282–293.
- (6) Larsson, L.; Decker, A. M.; Nibali, L.; Pilipchuk, S. P.; Berglundh, T.; Giannobile, W. V. Regenerative Medicine for Periodontal and Peri-Implant Diseases. *J. Dent. Res.* **2016**, *95* (3), 255–266.
- (7) Zhao, R.; Yang, R.; Cooper, P. R.; Khurshid, Z.; Shavandi, A.; Ratnayake, J. Bone Grafts and Substitutes in Dentistry: A Review of Current Trends and Developments. *Molecules* **2021**, *26* (10), 3007.
- (8) Yamada, M.; Egusa, H. Current Bone Substitutes for Implant Dentistry. *J. Prosthodont Res.* **2018**, *62* (2), 152–161.
- (9) Li, Y.; Ling, J.; Jiang, Q. Inflammation in Alveolar Bone Loss. *Front Immunol* **2021**, *12*, No. 691013.
- (10) Hathaway-Schrader, J. D.; Novince, C. M. Maintaining Homeostatic Control of Periodontal Bone Tissue. *Periodontol* **2021**, *86* (1), 157–187.
- (11) Henderson, B.; Kaiser, F. Bacterial Modulators of Bone Remodeling in the Periodontal Pocket. *Periodontol* **2018**, *76* (1), 97–108.
- (12) Kharbikar, B. N.; Mohindra, P.; Desai, T. A. Biomaterials to Enhance Stem Cell Transplantation. *Cell Stem Cell* **2022**, *29* (5), 692–721.
- (13) Wu, J.; Pan, Z.; Zhao, Z.-Y.; Wang, M.-H.; Dong, L.; Gao, H.-L.; Liu, C.-Y.; Zhou, P.; Chen, L.; Shi, C.-J.; Zhang, Z.-Y.; Yang, C.; Yu, S.-H.; Zou, D.-H. Anti-Swelling, Robust, and Adhesive Extracellular Matrix-Mimicking Hydrogel Used as Intraoral Dressing. *Adv. Mater.* **2022**, *34* (20), No. 2200115.
- (14) Tian, Y.; Li, Y.; Liu, J.; Lin, Y.; Jiao, J.; Chen, B.; Wang, W.; Wu, S.; Li, C. Photothermal Therapy with Regulated Nrf2/NF- κ B Signaling Pathway for Treating Bacteria-Induced Periodontitis. *Bioact. Mater.* **2022**, *9*, 428–445.
- (15) Um, S.; Lee, J.-H.; Seo, B.-M. TGF- β 2 Downregulates Osteogenesis under Inflammatory Conditions in Dental Follicle Stem Cells. *Int. J. Oral Sci.* **2018**, *10* (3), 29.
- (16) Sczepanik, F. S. C.; Grossi, M. L.; Casati, M.; Goldberg, M.; Glogauer, M.; Fine, N.; Tenenbaum, H. C. Periodontitis Is an Inflammatory Disease of Oxidative Stress: We Should Treat It That Way. *Periodontol* **2020**, *84* (1), 45–68.
- (17) Meng, Z.; Liu, J.; Feng, Z.; Guo, S.; Wang, M.; Wang, Z.; Li, Z.; Li, H.; Sui, L. N-Acetylcysteine Regulates Dental Follicle Stem Cell Osteogenesis and Alveolar Bone Repair via ROS Scavenging. *Stem Cell Res. Ther.* **2022**, *13* (1), 466.
- (18) Sun, H.; Xu, J.; Wang, Y.; Shen, S.; Xu, X.; Zhang, L.; Jiang, Q. Bone Microenvironment Regulative Hydrogels with ROS Scavenging and Prolonged Oxygen-Generating for Enhancing Bone Repair. *Bioact. Mater.* **2023**, *24*, 477–496.
- (19) Liu, M.; Wu, X.; Cui, Y.; Liu, P.; Xiao, B.; Zhang, X.; Zhang, J.; Sun, Z.; Song, M.; Shao, B.; Li, Y. Mitophagy and Apoptosis Mediated by ROS Participate in AlCl₃-Induced MC3T3-E1 Cell Dysfunction. *Food Chem. Toxicol.* **2021**, *155*, No. 112388.
- (20) Weng, Y.; Wang, H.; Li, L.; Feng, Y.; Xu, S.; Wang, Z. Trem2-Mediated Syk-Dependent ROS Amplification Is Essential for

Osteoclastogenesis in Periodontitis Microenvironment. *Redox Biol.* **2021**, *40*, No. 101849.

(21) Dhada, K. S.; Hernandez, D. S.; Suggs, L. J. In Vivo Photoacoustic Tracking of Mesenchymal Stem Cell Viability. *ACS Nano* **2019**, *13* (7), 7791–7799.

(22) Jiang, Y.; Zhang, P.; Zhang, X.; Lv, L.; Zhou, Y. Advances in Mesenchymal Stem Cell Transplantation for the Treatment of Osteoporosis. *Cell Prolif* **2021**, *54* (1), No. e12956.

(23) Guo, Z.; Yang, C.-T.; Chien, C.-C.; Selth, L. A.; Bagnaninchi, P. O.; Thierry, B. Optical Cellular Micromotion: A New Paradigm to Measure Tumor Cells Invasion within Gels Mimicking the 3D Tumor Environments. *Small Methods* **2022**, *6* (8), No. 2200471.

(24) Guo, Z.; Yang, C.-T.; Maritz, M. F.; Wu, H.; Wilson, P.; Warkiani, M. E.; Chien, C.-C.; Kempson, I.; Aref, A. R.; Thierry, B. Validation of a Vasculogenesis Microfluidic Model for Radiobiological Studies of the Human Microvasculature. *Advanced Materials Technologies* **2019**, *4* (4), No. 1800726.

(25) Han, X.; Tang, S.; Wang, L.; Xu, X.; Yan, R.; Yan, S.; Guo, Z.; Hu, K.; Yu, T.; Li, M.; Li, Y.; Zhang, F.; Gu, N. Multicellular Spheroids Formation on Hydrogel Enhances Osteogenic/Odontogenic Differentiation of Dental Pulp Stem Cells Under Magnetic Nanoparticles Induction. *Int. J. Nanomedicine* **2021**, *16*, 5101–5115.

(26) Qin, Z.; Li, Y.; Gu, N. Progress in Applications of Prussian Blue Nanoparticles in Biomedicine. *Adv. Healthc Mater.* **2018**, *7* (20), No. e1800347.

(27) Komkova, M. A.; Karyakina, E. E.; Karyakin, A. A. Catalytically Synthesized Prussian Blue Nanoparticles Defeating Natural Enzyme Peroxidase. *J. Am. Chem. Soc.* **2018**, *140* (36), 11302–11307.

(28) Wang, Y.; Liang, Z.; Liang, Z.; Lv, W.; Chen, M.; Zhao, Y. Advancements of Prussian Blue-Based Nanoplatfroms in Biomedical Fields: Progress and Perspectives. *J. Controlled Release* **2022**, *351*, 752–778.

(29) Kim, T.; Lemaster, J. E.; Chen, F.; Li, J.; Jokerst, J. V. Photoacoustic Imaging of Human Mesenchymal Stem Cells Labeled with Prussian Blue-Poly(L-Lysine) Nanocomplexes. *ACS Nano* **2017**, *11* (9), 9022–9032.

(30) Busquets, M. A.; Estelrich, J. Prussian Blue Nanoparticles: Synthesis, Surface Modification, and Biomedical Applications. *Drug Discov Today* **2020**, *25* (8), 1431–1443.

(31) Estelrich, J.; Busquets, M. A. Prussian Blue: A Nanozyme with Versatile Catalytic Properties. *Int. J. Mol. Sci.* **2021**, *22* (11), 5993.

(32) Zhang, W.; Wang, J.; Xie, Z.; Zou, H.; Chen, Q.; Xu, L.; Hu, L.; Fang, N.; Xu, J.; Zhou, J.; Liu, J.; Ran, H.; Wang, Z.; Zhang, Y.; Guo, D. Antithrombotic Therapy by Regulating the ROS-Mediated Thrombosis Microenvironment and Specific Nonpharmaceutical Thrombolysis Using Prussian Blue Nanodroplets. *Small* **2022**, *18* (15), No. 2106252.

(33) Zhou, Q.; Yang, H.; Chen, X.; Xu, Y.; Han, D.; Zhou, S.; Liu, S.; Shen, Y.; Zhang, Y. Cascaded Nanozyme System with High Reaction Selectivity by Substrate Screening and Channeling in a Microfluidic Device. *Angew. Chem., Int. Ed. Engl.* **2022**, *61* (2), No. e202112453.

(34) Zhang, Y.; Peng, L.; Hu, K.; Gu, N. Stress Relaxation-Induced Colon Tumor Multicellular Spheroid Culture Based on Biomimetic Hydrogel for Nanoenzyme Ferroptosis Sensitization Evaluation. *Adv. Healthc. Mater.* **2023**, *12* (3), No. 2202009.

(35) Zhang, M.; Yan, S.; Xu, X.; Yu, T.; Guo, Z.; Ma, M.; Zhang, Y.; Gu, Z.; Feng, Y.; Du, C.; Wan, M.; Hu, K.; Han, X.; Gu, N. Three-Dimensional Cell-Culture Platform Based on Hydrogel with Tunable Microenvironmental Properties to Improve Insulin-Secreting Function of MIN6 Cells. *Biomaterials* **2021**, *270*, No. 120687.

(36) Oddo, E.; Pesce, R. M.; Derudi, M.; Magagnin, L. Amino-Functionalized Magnetic Nanoparticles for CO₂ Capture. *International Journal of Smart and Nano Materials* **2021**, *12* (4), 472–490.

(37) Hu, K.; Sun, J.; Guo, Z.; Wang, P.; Chen, Q.; Ma, M.; Gu, N. A Novel Magnetic Hydrogel with Aligned Magnetic Colloidal Assemblies Showing Controllable Enhancement of Magnetothermal Effect in the Presence of Alternating Magnetic Field. *Adv. Mater.* **2015**, *27* (15), 2507–2514.

(38) Hu, K.; Zhou, N.; Li, Y.; Ma, S.; Guo, Z.; Cao, M.; Zhang, Q.; Sun, J.; Zhang, T.; Gu, N. Sliced Magnetic Polyacrylamide Hydrogel with Cell-Adhesive Microarray Interface: A Novel Multicellular Spheroid Culturing Platform. *ACS Appl. Mater. Interfaces* **2016**, *8* (24), 15113–15119.

(39) Tan, J.; Wu, S.; Cai, Q.; Wang, Y.; Zhang, P. Reversible Regulation of Enzyme-like Activity of Molybdenum Disulfide Quantum Dots for Colorimetric Pharmaceutical Analysis. *J. Pharm. Anal.* **2022**, *12* (1), 113–121.

(40) Zhang, Q.; Luo, P.; Zheng, L.; Chen, J.; Zhang, J.; Tang, H.; Liu, D.; He, X.; Shi, Q.; Gu, L.; Li, J.; Guo, Q.; Yang, C.; Wong, Y. K.; Xia, F.; Wang, J. 18beta-Glycyrrhetic Acid Induces ROS-Mediated Apoptosis to Ameliorate Hepatic Fibrosis by Targeting PRDX1/2 in Activated HSCs. *J. Pharm. Anal.* **2022**, *12* (4), 570–582.

(41) Zhang, W.; Hu, S.; Yin, J.-J.; He, W.; Lu, W.; Ma, M.; Gu, N.; Zhang, Y. Prussian Blue Nanoparticles as Multienzyme Mimetics and Reactive Oxygen Species Scavengers. *J. Am. Chem. Soc.* **2016**, *138* (18), 5860–5865.

(42) Gan, L.; Li, B.; Guo, M.; Weng, X.; Wang, T.; Chen, Z. Mechanism for Removing 2,4-Dichlorophenol via Adsorption and Fenton-like Oxidation Using Iron-Based Nanoparticles. *Chemosphere* **2018**, *206*, 168–174.

(43) Hu, Z.-C.; Lu, J.-Q.; Zhang, T.-W.; Liang, H.-F.; Yuan, H.; Su, D.-H.; Ding, W.; Lian, R.-X.; Ge, Y.-X.; Liang, B.; Dong, J.; Zhou, X.-G.; Jiang, L.-B. Piezoresistive MXene/Silk Fibroin Nanocomposite Hydrogel for Accelerating Bone Regeneration by Re-Establishing Electrical Microenvironment. *Bioact. Mater.* **2023**, *22*, 1–17.

(44) Hasani-Sadrabadi, M. M.; Sarrion, P.; Pouraghaei, S.; Chau, Y.; Ansari, S.; Li, S.; Aghaloo, T.; Moshaverinia, A. An Engineered Cell-Laden Adhesive Hydrogel Promotes Craniofacial Bone Tissue Regeneration in Rats. *Sci. Transl. Med.* **2020**, *12* (534), No. eaay6853.

(45) Xue, S.; Tang, N.; Zhou, C.; Fang, S.; Haick, H.; Sun, J.; Wu, X. Anti-Wound Dehiscence and Antibacterial Dressing with Highly Efficient Self-Healing Feature for Guided Bone Regeneration Wound Closure. *Adv. Healthc Mater.* **2024**, *13*, No. 2304128.

(46) Kim, W.; Gwon, Y.; Park, S.; Kim, H.; Kim, J. Therapeutic Strategies of Three-Dimensional Stem Cell Spheroids and Organoids for Tissue Repair and Regeneration. *Bioact. Mater.* **2023**, *19*, 50–74.

(47) Kang, S.-M.; Kim, D.; Lee, J.-H.; Takayama, S.; Park, J. Y. Engineered Microsystems for Spheroid and Organoid Studies. *Adv. Healthc Mater.* **2021**, *10* (2), No. e2001284.

(48) Tarasov, V. V.; Svistunov, A. A.; Chubarev, V. N.; Dostdar, S. A.; Sokolov, A. V.; Brzecka, A.; Sukocheva, O.; Neganova, M. E.; Klockhov, S. G.; Somasundaram, S. G.; Kirkland, C. E.; Aliev, G. Extracellular Vesicles in Cancer Nanomedicine. *Semin Cancer Biol.* **2021**, *69*, 212–225.

(49) Kim, T.; Lee, N.; Arifin, D. R.; Shats, I.; Janowski, M.; Walczak, P.; Hyeon, T.; Bulte, J. W. M. In Vivo Micro-CT Imaging of Human Mesenchymal Stem Cells Labeled with Gold-Poly-L-Lysine Nanocomplexes. *Adv. Funct. Mater.* **2017**, *27* (3), No. 1604213.

(50) Lim, S.; Yoon, H. Y.; Jang, H. J.; Song, S.; Kim, W.; Park, J.; Lee, K. E.; Jeon, S.; Lee, S.; Lim, D.-K.; Kim, B.-S.; Kim, D.-E.; Kim, K. Dual-Modal Imaging-Guided Precise Tracking of Bioorthogonally Labeled Mesenchymal Stem Cells in Mouse Brain Stroke. *ACS Nano* **2019**, *13* (10), 10991–11007.